

Origin of depressed fill factor in organic solar cells due to S-shape current-voltage characteristics

Cite as: J. Appl. Phys. 127, 053101 (2020); doi: 10.1063/1.5131355

Submitted: 15 October 2019 · Accepted: 14 January 2020 ·

Published Online: 3 February 2020



Aniket Rana,^{1,2,a)} Amit Kumar,^{1,3} Nikita Vashistha,^{1,3} Kuldeep K. Garg,^{1,3} Suresh Chand,³ and Rajiv K. Singh^{1,3,a)}

AFFILIATIONS

¹Academy of Scientific and Innovative Research (AcSIR), CSIR-NPL Campus, New Delhi 110012, India

²Indian Institute of Technology Delhi, Hauz Khas, New Delhi 110016, India

³CSIR—National Physical Laboratory, Dr. K. S. Krishnan Marg, New Delhi 110012, India

^{a)}Authors to whom correspondence should be addressed: aniket.rana@gmail.com and rajivsingh@nplindia.org

ABSTRACT

Often, a depressed fill factor is observed in organic solar cells (OSCs), which is usually known as S-shaped current-voltage (J–V) characteristics. To investigate the origin of the depressed fill factor further, a poly[N-9-heptadecan-2,7-carbazole-alt-5,5-(4,7-di-2-thienyl-2,1,3-benzothiadiazole)]:[6,6]-phenyl C71 butyric acid methyl ester based OSC has been characterized through impedance spectroscopy. In addition, the photocurrent vs the applied effective bias plot reveals that the S-shaped J–V characteristics primarily reduce the diffusion current of the device. The present study shows that the diffusion current dominated section of photocurrent reduces with a slope of 2 in the depressed fill factor section given that the slope may further increase as per the impact of the S-shape. The reduction in the diffusion constant (D_n) in the S-shaped region supports the decrease in the diffusion current, which is observed through the photocurrent analysis. It is observed that, in the S-shaped section of the current-voltage characteristics, the transport time for free carriers increases up to 443 μ s. The larger Urbach energy for the active layer of an S-shaped device demonstrates higher subbandgap disorder. Therefore, it is concluded that the accumulation of the charge carriers within the device and disorder in the active layer leads to the S-shaped current-voltage characteristics as well as poor carrier extraction.

Published under license by AIP Publishing. <https://doi.org/10.1063/1.5131355>

I. INTRODUCTION

The new advancement in research and development of organic solar cells (OSCs) has demonstrated the potential power conversion efficiency to compete with the conventional photovoltaic technology. As a result, recently, Meng *et al.* have reported a 17.3% efficiency in a multijunction tandem configuration.¹ OSCs are a promising candidate with the viable technology to meet the world's rising energy demand. The main hurdle faced by this technology is the efficiency and stability; in particular, better understanding of such devices will lead to increased performance with reduced costs and manufacturing efforts.^{2–4} One of the significant advantages of the organic solar cells, while comparing with inorganic solar cells, is the possibility for the fabrication on flexible substrates via low-cost roll-to-roll printing and coating processes.^{5–7} Despite its advantages, sometimes, the performance of OSCs is limited by the depressed fill factor (FF). This limitation may occur due to the S-shaped J–V characteristics. However, fast nonradiative recombination and mobility imbalance could also lead to the depressed fill factor without invoking S-shaped

characteristics.⁸ There are many reports available on S-shaped J–V characteristics for the OSCs, wherein Gupta *et al.* suggested that the appearance of an S-shape in J–V characteristics is the signature of a counterinjecting diode that occurs due to the charge accumulation near one of the electrodes,^{9,10} whereas Glatthaar *et al.* used impedance spectroscopy measurements to investigate OSCs and proposed that the problem involved in diminishing charge carrier extraction due to defects at the cathode interface leads to S-shaped J–V curves.¹¹ Tress *et al.* argued that an imbalance of the individual charge carrier mobility would induce S-shaped J–V curves in planar heterojunction OSCs.¹² The effect of diffusion current as a driving force for charge extraction can also lead to the formation of S-shaped J–V curves in OSCs, which has been shown by transient photocurrent measurements.¹³ Due to various justifications, the exact origin of the S-shaped effect in the OSC is still under discussion. As a result, the effect has not been experimentally understood unambiguously yet. Therefore, a detailed study is presented to understand and validate the main reasons for the origin of S-shaped J–V

characteristics in OSCs using impedance spectroscopy and photocurrent analysis. Impedance spectroscopy measurements are performed on the OSC to get a closer insight into charge distribution, recombination, and trapping dynamics.^{14,15} A simple AC equivalent circuit model has been used to analyze the impedance data acquired from devices over a range of bias voltages from 0 V to 0.9 V in the dark conditions and 100 mW/cm² in illuminated conditions. The AC equivalent circuit model is used as a tool to localize and quantify the involved loss mechanisms at interfaces of the devices that has revealed the origin of the depressed fill factor in OSCs. The diffusion and drift current extracted from photocurrent determine the impact of the S-shaped nature in the device's J-V characteristics.

II. EXPERIMENTAL

The active layer solution was prepared by mixing trichlorobenzene (TCB) and chlorobenzene (CB) in a 3:1 volume ratio, whereas 7 mg/ml solution of poly[N-9-heptadecanyl-2,7-carbazole-alt-5,5-(4,7-di-2-thienyl-2,1,3-benzothiadiazole)] (PCDTBT) and 28 mg/ml solution of [6,6]-phenyl C71 butyric acid methyl ester (PC71BM) in a TCB:CB solvent was kept inside the nitrogen filled glovebox separately. These solutions were left overnight stirring at 60 °C on a hot plate. The final 35 mg/ml solution for device fabrication was achieved by mixing the PCDTBT and PC71BM solution together. The active layer was spin-coated on a predeposited MoO₃ on an indium tin oxide glass (ITO) substrate at 800 rpm for 60 s inside the glovebox; after that, the resulting film was annealed at 70 °C for 10 min on a hot plate. Before coating the materials, the ITO substrate was prepared by patterning with a laser scribe and subsequently cleaned in detergent solution, acetone, and isopropanol followed by UV ozone treatment for 10 min. The 8 nm MoO₃ layer was thermally deposited at a 1×10^{-6} mbar pressure with a 0.2 Å/s rate. Aluminum as a cathode was also thermally evaporated in a 1×10^{-6} mbar pressure with a 0.5 Å/s rate of deposition to achieve 100 nm thicknesses. The final device structure is achieved as ITO/MoO₃/PCDTBT:PC71BM/Al. The controlled introduction of the S-shape in device A was achieved

by increasing the thickness of the active layer by reducing the spin coating speed for the active layer by 200 rpm. The thickness difference between the active layer of device A and device B are given in Fig. S1 in the [supplementary material](#). The J-V characterization was recorded under dark conditions as well as at 1 sun illumination intensity using a Keithley 4200 semiconductor analyzer. Impedance spectroscopy measurement was performed by an Autolab PGSTAT302N under 1 sun illumination and dark conditions. The AC signal for impedance measurement was 40 mV to achieve a good signal to noise ratio. A solar simulator AM 1.5G (Class AAA, Photo Emission Tech.) was used for the illumination purpose.

III. RESULTS AND DISCUSSION

The illuminated J-V characteristics of the OSC (device A) in Fig. 1(a) shows an S-shape in the applied voltage range of 0.5 V–1.0 V leading to a 38% fill factor (FF). The efficiency and open circuit voltage (V_{oc}) of device A is 2% and 0.92 V, respectively. The dark J-V characteristics recommends that the S-shape occurs in the space charge dominated region of device A.¹⁶ However, it is hard to predict the S-shaped feature in the solar cell just by observing only dark J-V characteristics, whereas Fig. 1(b) shows the J-V characteristics of without S-shaped OSCs (device B). The efficiency, open circuit voltage, and FF of device B is 2.06%, 0.88 V, and 45.6%, respectively.

The S-shape predominantly appears in the illuminated J-V curve which implies that it is related to the photocurrent in the device as well. Therefore, we have estimated the photocurrent (J_{ph}) by subtracting the dark current from the light current ($J_{ph} = J_L - J_D$) and plotted against the effective applied bias V_{eff} ($V_0 - V$) on a logarithmic scale for both device A (with an S-shape) and device B (without an S-shape), where V_0 is the compensation voltage at which dark and light current are equal ($J_L = J_D$), and it is almost equal to the built-in potential of OSCs,^{17,18} whereas device B does not show any S-shaped curve. Here, the effective applied bias shows the strength of the electric field inside the device.

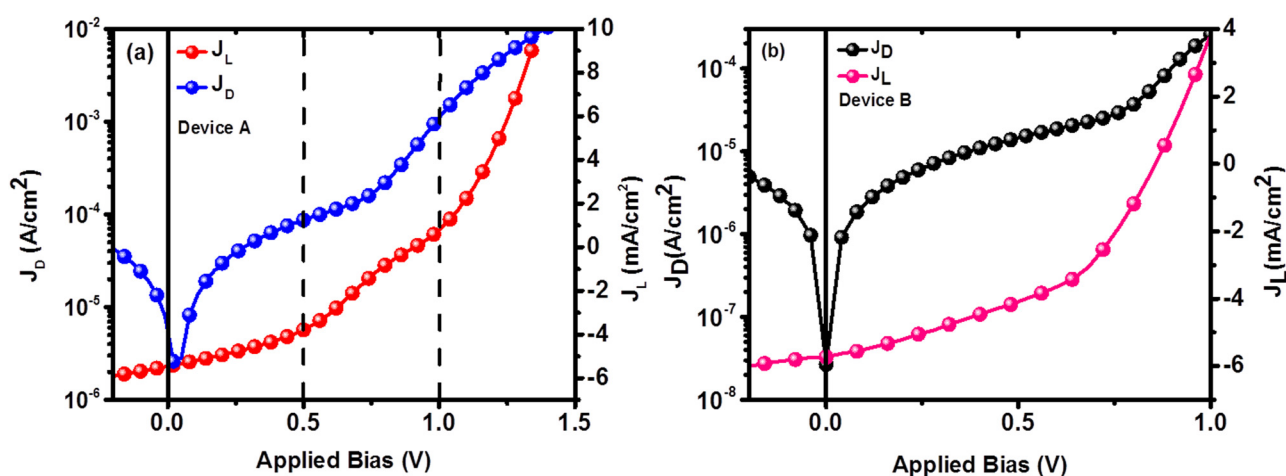


FIG. 1. (a) Dark and illuminated current-voltage characteristics of an S-shaped OSC and (b) without an S-shaped OSC.

Usually, such a plot has two prominent regions called diffusion and drift corresponding to low and high electric fields, respectively, and are outlined in Fig. 1(b)¹⁹ by vertical dotted lines. In device A, the photocurrent up to 0.65 V effective bias appears due to the diffusion current; and beyond $V_0 - V > 0.65$ V, the drift current dominates. Typically, in the OSC without S-shaped characteristics, the diffusion dominated photocurrent has a slope around unity.²⁰ In device A, at the low effective bias ($V_0 - V < 0.24$ V), photocurrent increases linearly; therefore, in this region, the slope is unity ($S = 1$); and after that, the diffusion current slope changes to 2. If we compare the depressed fill factor region of Fig. 1(a) to the photocurrent vs the effective bias plot in Fig. 2, the plot section having a slope of 2 represents the S-shaped region, which means that the photocurrent changes more rapidly in this region. The first inflection point in the curve can be observed at 0.24 V, which reflects the voltage around V_{oc} ($V_{eff} = 0.24$ V) in the J-V characteristics, is where the S-shaped curve ends. The beginning of S-shape occurrence in J-V curve can be observed in J_{ph} vs V_{eff} plot at 0.65 V, which is a second inflection point. This recommends that the appearance of S-shape rapidly reduces the diffusion current in the device (device A), whereas devices without S-shape do not allow rapid reduction in diffusion current, as can be observed for device B. It occurs because of the reduced internal field and poor charge extraction from the electrodes.²¹ The sharp decrease in the diffusion current is also an indication of high recombination of charge carriers in the device at the internal interfaces (donor-acceptor, active layer-hole transport layer, metal interface).¹³

Furthermore, the poor carrier extraction and injection behavior through the electrodes as well as the hole transport layer effect leading to the depressed FF in device A have been investigated through impedance spectroscopy under dark and illuminated conditions as given in Figs. 3(a) and 3(b). Figures 3(a)–3(d) show the impedance spectra for with S-shaped OSCs and without S-shaped OSCs under dark conditions. To identify the changes in transport and bulk material properties in both devices, the frequency range is selectively chosen from 10 Hz to 1 MHz, keeping the forward bias voltage variation from 0 V to 0.9 V to investigate the injection and

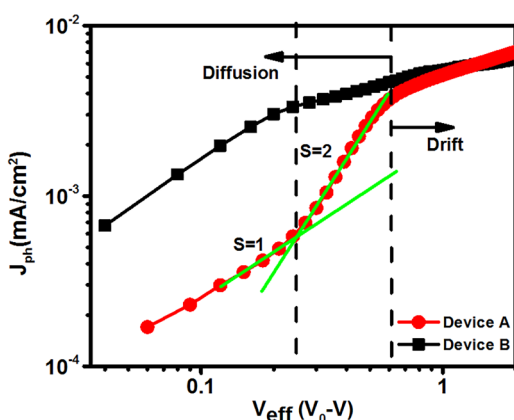


FIG. 2. Photocurrent vs effective bias plot for device A (with an S-shape) and device B (without an S-shape) depicting the drift and diffusion current in devices.

transport behavior of the devices. The self-extraction and accumulation of charge carriers inside the devices have been validated by performing the impedance measurement under 100 mW illumination intensity and 0 V biasing conditions. The two parallel combinations of resistance and constant phase element ($R||CPE$) connected in series together with another resistance R in series ($R-R_t||CPE_t-R_{\mu}||CPE_{\mu}$) can characterize the true AC behavior of charge carrier dynamics in the dark as well as in the illuminated OSC which are shown in Fig. 3(e). The first parallel combination of $R_t||CPE_t$ signifies contact and transport properties in devices, which is indicated in the high frequency segment of the Nyquist plot.²² The calculation of time constant (τ_t) from this combination provides characteristic transport time of the photogenerated carriers under illuminated conditions and injected charge carriers inside the device under the dark condition, respectively. R_t originates from the material interface resistance between the polymer/transport layer and polymer/metal electrode, whereas the transport capacitance (CPE_t) originates from the polarization of mobile charge carriers at the interface of interlayers before the extraction from the respective electrodes. The evaluated transport time is independent of the applied voltage, rather it depends upon diffusion-recombination between nonabsorbing contacts, but the unusual diffusion-recombination due to the accumulation of charge carriers within the interfaces of devices can modify the transport time with an applied bias.²³ The bulk property of the device is represented by the $R_{\mu}||CPE_{\mu}$ combination in the equivalent circuit, where R_{μ} is originated from the bulk resistance of the device, and the capacitance evaluated from CPE_{μ} commonly known as chemical capacitance (C_{μ}) originated from the polarization and accumulation of charge carriers created at the donor-acceptor interface and it describes the available free charge carrier density in the device.²⁴ The charge accumulation at the interface of the active layer and hole transport layer or the metal electrode interfaces also contribute to the population of intra-gap states present in the active material where they are stockpiled and disturb the internal field of the device. Here, the constant phase element (CPE) is an empirical circuit element and its impedance is given by $Z_{CPE} = A(j\omega)^{-\alpha}$. It is a leaking capacitor and turns as an ideal capacitor when $\alpha = 1$ and equivalent to a resistor when $\alpha = 0$. The characteristic exponent α specifies the degree of imperfection of an ideal capacitive element ($0 < \alpha \leq 1$).^{25,26} Nonideal behaviors caused by the trap states present in the bulk of the intrinsic active material like inhomogeneity in the active material, interface material, and origin of nonideal behavior at the molecular level can also be represented by the CPE. In the present study, α_t for device A remains very close to 1, whereas α_{μ} is marginally smaller than α_t . However, for device B, both α_{μ} and α_t remain very close to 1 as can be observed in Table S1 in the supplementary material. It indicates that the bulk property also contributed to the nonideal behavior of J-V characteristics, i.e., S-shaped feature. The transport time (τ_t) has been used to estimate the charge carrier mobility (μ_n) by the Nernst-Einstein relationship in the device, which is given as²³

$$\mu_n = \frac{qD_n}{K_B T}, \quad (1)$$

where $K_B T$ is the thermal voltage, D_n ($= \frac{L^2}{\tau_t}$) is the electron diffusivity, and L is the active layer thickness.

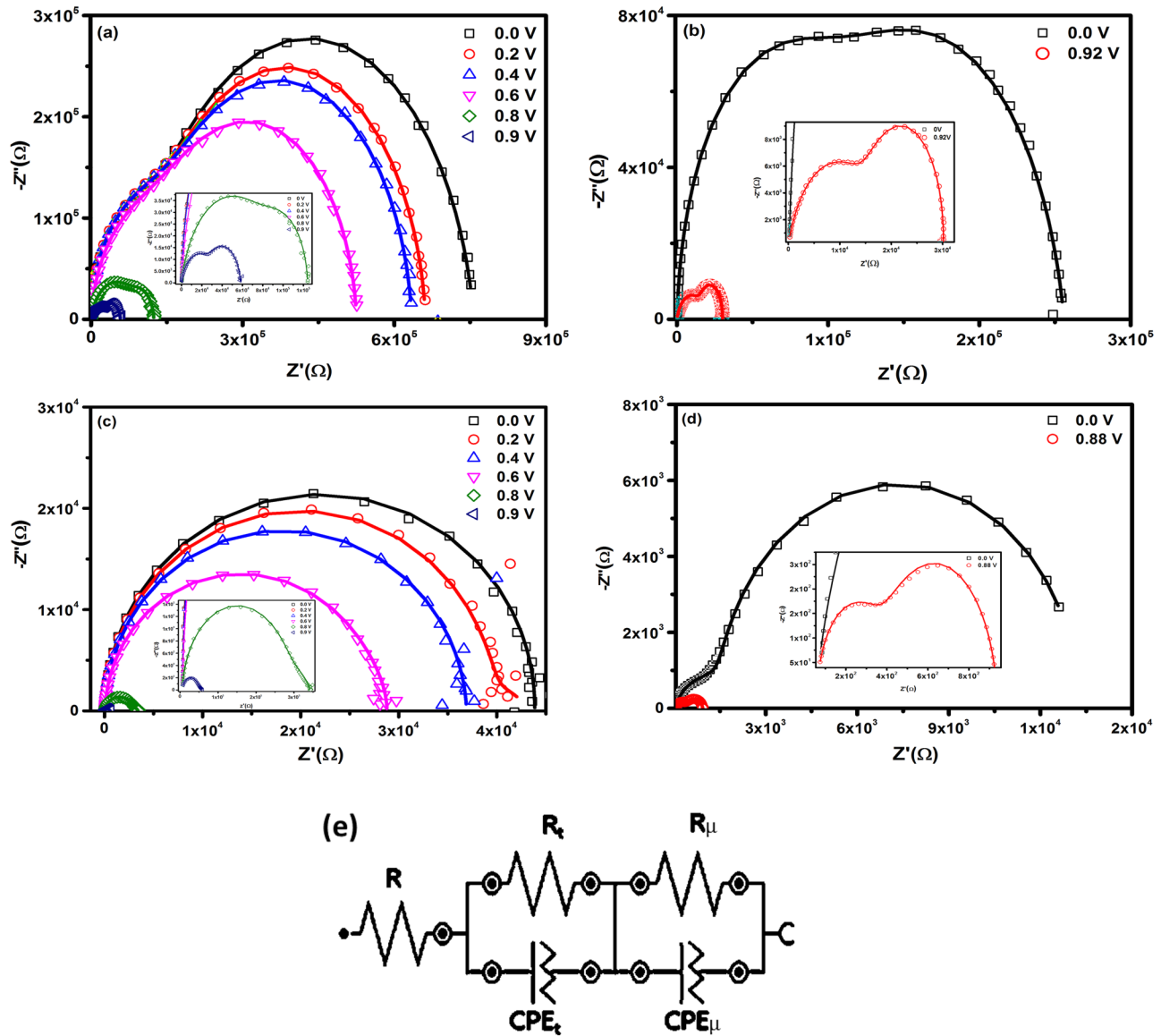


FIG. 3. Nyquist plot for (a) device A under dark conditions, (b) device A under illuminated conditions, (c) device B under dark conditions, and (d) device B under illuminated conditions. Symbols and continuous lines indicate the experimental and fitting data, respectively. The inset of each figure shows the high frequency region of the Nyquist plot. and (e) shows the equivalent AC circuit model for experimental data fitting and parameter evaluation.

Taking into account the voltage dependent dark impedance measurements in Fig. 3(a), the applied voltage in the range of 0.4 V–0.8 V is contemporary with the occurrence of the S-shaped J–V curve in device A. The impedance plot shows that the R_{tL} reduces with the increment in applied bias; however, the large change is not observed in R_{tL} for the bias voltage of 0.2 V and 0.4 V which lies at the starting of the S-shaped region. The small change in R_{tL} irrespective of the increased bias voltage is caused by the reduced diffusion current in the device due to the injection barrier

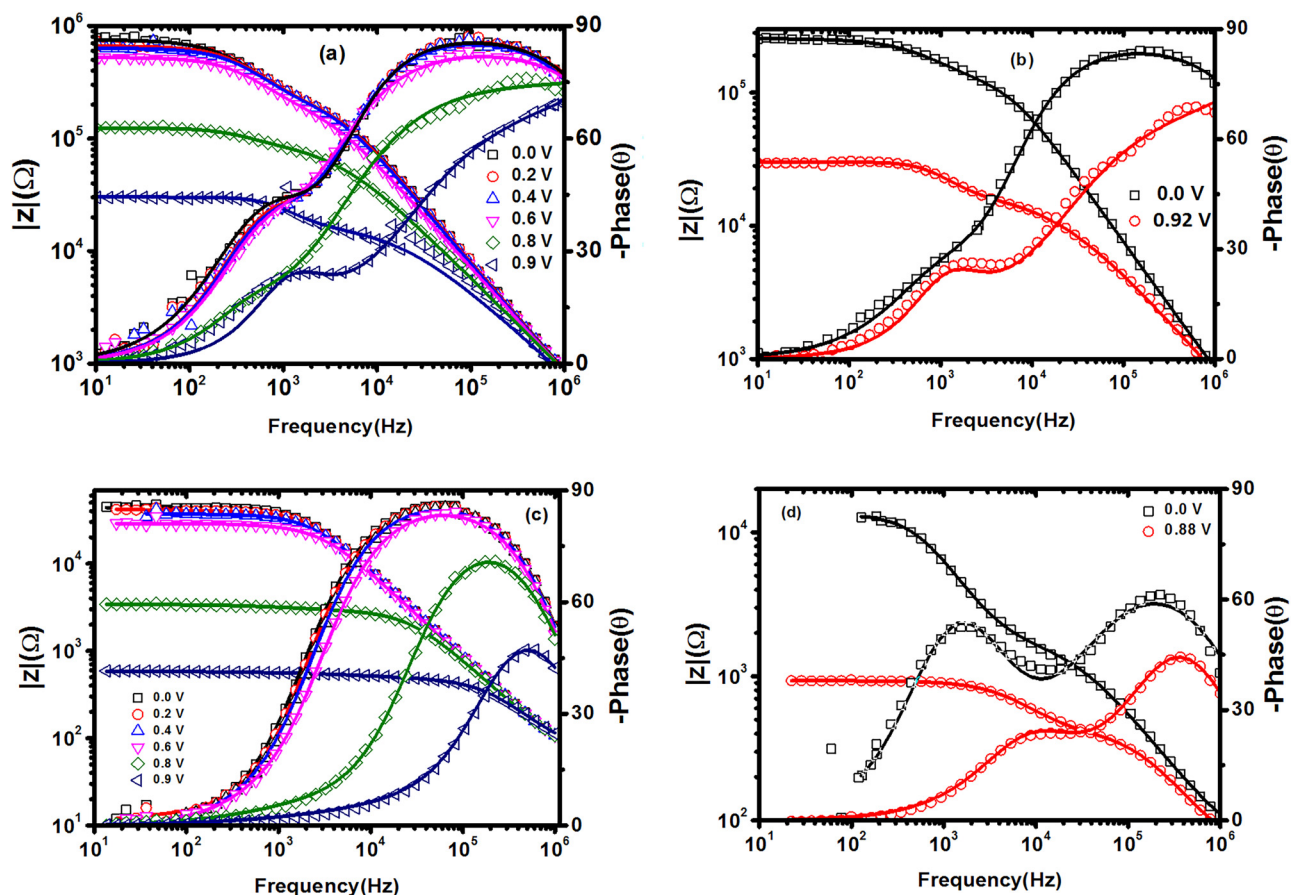
formed by the accumulated carriers at the interface. The fact that the carriers are accumulated and forming barrier at the interface can also be inferred by the small increment in the chemical capacitance C_{μ} , which is 0.96 nF at 0.4 V and for 0.6 V it becomes 1.19 nF. The accumulated charge carriers also affect the transport time (τ_t) in the device, which can be observed from Table 1. On the other hand, the impedance spectra of device B under dark conditions [Fig. 3(d)] show smaller resistance compared to device A and the change in R_{tL} at 0.4 V as compared to 0.2 V is almost two

TABLE I. Transport time, diffusion constant, and electron mobility evaluated from the impedance spectroscopy for device A (S-shape) and device B (without an S-shape) at different applied bias.

Device A (S-shape)		Dark				
Applied bias (V)	0.0	0.2	0.4	0.6	0.8	0.9
τ_t (s)	2.66×10^{-5}	4.02×10^{-5}	4.26×10^{-5}	5.22×10^{-5}	4.43×10^{-4}	1.32×10^{-5}
D_n (cm ² s ⁻¹)	3.75×10^{-6}	2.49×10^{-6}	2.35×10^{-6}	1.92×10^{-6}	2.26×10^{-7}	7.58×10^{-6}
μ_n (cm ² V ⁻¹ s ⁻¹)	1.44×10^{-4}	9.57×10^{-5}	9.04×10^{-5}	7.37×10^{-5}	8.68×10^{-6}	2.92×10^{-4}
Device B (without an S-shape)		Dark				
τ_t (s)	6.62×10^{-5}	4.37×10^{-5}	9.19×10^{-5}	3.7×10^{-5}	6.07×10^{-5}	3.14×10^{-5}
D_n (cm ² s ⁻¹)	7.83×10^{-7}	1.19×10^{-6}	5.64×10^{-7}	1.4×10^{-6}	8.55×10^{-7}	1.65×10^{-6}
μ_n (cm ² V ⁻¹ s ⁻¹)	3.0×10^{-5}	4.57×10^{-5}	2.17×10^{-5}	5.40×10^{-4}	3.29×10^{-5}	6.34×10^{-5}

times larger. The variation in the transport time in device A up to 0.6 V is minor; however, at 0.8 V, it becomes $443 \mu\text{s}$, which is one order higher compared to the other bias as well as with device B. It indicates that the accumulated charge carriers at the interface

influence the transport properties in devices which can be observed in device A in Table S1 in the [supplementary material](#) as a two order increment in C_t with respect to the bias voltage. Similarly, the diffusion constant (D_n) is also reduced one order in the

**FIG. 4.** The Bode plot of impedance and phase under different bias for (a) device A under dark conditions, (b) device A under illuminated conditions, (c) device B under dark conditions, and (d) device B under illuminated conditions.

S-shaped region; therefore, the steep variation in the diffusion current is observed as shown in Fig. 1(b). At 0.2 V, D_n is $2.49 \times 10^{-6} \text{ cm}^2 \text{ s}^{-1}$ which is further one order reduced to $2.26 \times 10^{-7} \text{ cm}^2 \text{ s}^{-1}$ at 0.8 V. These findings support the reduction in diffusion current in the device which is also observed in the photocurrent vs effective applied bias calculation. The Nyquist plot for device A under the illuminated condition is given in Fig. 3(b) for 0 V and 0.92 V (V_{oc}). It can be observed that the first semicircle which correspond to the transport property in devices occurs at a much lower frequency compared to device B [Fig. 3(e)]. In this case, an imbalance in the carrier mobility is also observed in device A, in the depressed fill factor region, the mobility is reduced, whereas in device B, the mobility remains almost constant for all applied voltages. The similar observation has been also observed by Wagenpfahl *et al.*²⁷ The Bode plot shows the plot between the phase angle and the logarithm of the impedance modulus as a function of the logarithm of frequency. Unlike the Nyquist plot, the Bode plot explicitly shows the frequency information of the device. The decrease in the impedance with the increase in the frequency could be due to the slow dynamics relaxation process which is related to the stored charge within the device. The decrease in the impedance plateau in device A is observed from 100 Hz, whereas in device B, the impedance plateau starts decreasing from 1000 Hz as can be seen in Figs. 4(a) and 4(c). As the bias voltage is increased as in Fig. 4(a), the rise in the critical frequency and up to 0.8 V the decrease in the impedance plateau for device A [Fig. 4(a)] does not vary much, whereas for device B [Fig. 4(b)], the decrease in plateau is observed from more than 10 000 Hz. The increase in the critical frequency in the phase angle is observed due to the accumulation of carriers. A similar change in the phase angle is also observed in the illuminated Bode plot. For device A, two peaks are observed in the phase angle which corresponds to

the trapped carrier, whereas for device B, a single peak is observed which is due to the space charge carriers. Under illumination, two peaks are observed due to the generated photocarriers and space charge carriers within the device.

Furthermore, to get a more detailed physical understanding related to the structural disorder and fill factor decrement, UV–visible spectroscopy has been used to evaluate the Urbach energy (E_u),²⁸ as shown in Fig. 5. The relation between the absorption coefficient and Urbach energy is given as follows:^{29,30}

$$\alpha = \alpha_0 e^{\left(-\frac{E_g - h\nu}{E_u}\right)}, \quad (2)$$

where α_0 is the absorption on the band edge, $h\nu$ is the photon energy, E_g is the material bandgap, and E_u is called Urbach energy. In Fig. 5(a), the active layer film prepared for device A shows a slightly greater absorption as compared to the active layer film prepared for device B, which is due to the fact that more material is available to absorb the light. Urbach energy is an indicative parameter for structural disorder in semiconductors; and therefore in Fig. 5(b), the evaluated Urbach energy for the active layer of device A is 76.69 meV and for the active layer of device B is 48.03 meV. The absorption at the low photon energy occurs due to the available trap energy levels within the bandgap caused by subbandgap defects. Hence, by observing the absorption spectra at a lower photon energy, the magnitude of absorption suddenly increased for the active layer of device A as compared to device B by 28.66 meV, which indicates the larger available trap in the film fabricated at lower rpm causing S-shaped current–voltage curves. Furthermore, the morphology differences between the two films have been analyzed by Atomic Force Microscopy (AFM) as given in Fig. S2 of the [supplementary material](#). Figure S2(a) in the [supplementary material](#) shows the AFM image for

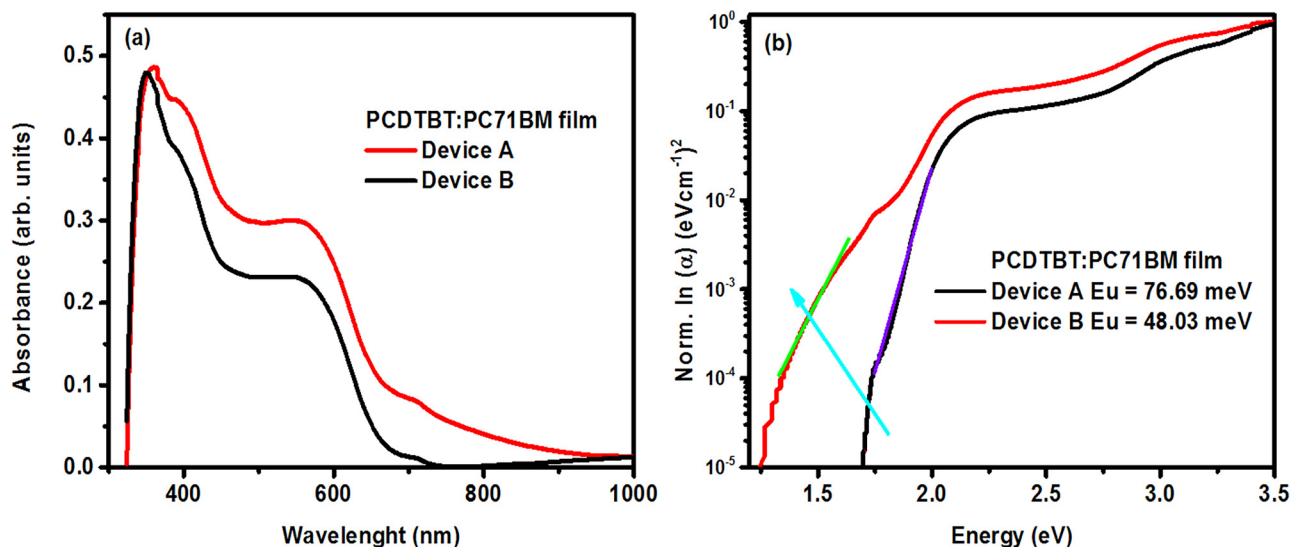


FIG. 5. (a) UV–visible absorption spectra and (b) evaluated Urbach energy for a PCDTBT:PC71BM film spin coated at 600 rpm (red line) (device A) and 800 rpm (black line) (device B).

the active layer film prepared for device A, whereas Fig. S2(b) in the [supplementary material](#) shows the AFM image for the active layer film coated for device B. The surface roughness (R_q) of the film coated for device A is 16.2 nm and of the film coated for device B is 12.1 nm. The slightly larger surface roughness of the film coated at lower speeds would lead to charge carrier loss as a recombination at the interface that caused the depression in the fill factor of the device.

IV. CONCLUSION

In summary, we have analyzed the cause of the depression in the fill factor in the organic solar cells due to the S-shaped characteristics by analyzing the photocurrent and impedance. From the photocurrent analysis, we have concluded that the S-shaped characteristics in device reduce the diffusion current, and the slope becomes 2 in the depressed fill factor section; that could change according to the impact of the S-shape. Impedance analysis confirms that the carrier accumulation causes depression in FFs in the organic solar cells. The reduction in the diffusion constant (D_n) in the S-shaped region supports the reduction in the diffusion current observed in the photocurrent analysis. The accumulation of the charge carriers inside the device increases the transport time of carriers up to 443 μ s. The thick active layer also creates the trap energy levels within the bandgap of the photoactive layer, leading to the depression in the fill factor.

SUPPLEMENTARY MATERIAL

See the [supplementary material](#) for the impedance parameters for device A and device B extracted after the AC equivalent circuit model fitting under dark conditions at different biasing conditions and also for a comparison of the thickness of the active layer and surface morphology from AFM.

ACKNOWLEDGMENTS

The authors thank the Director, National Physical Laboratory, Dr. K. S. Krishnan Marg, New Delhi, for his kind support. One of us, A. Rana, acknowledges CSIR, New Delhi, India for the award of the Research Associate Fellowship.

REFERENCES

- ¹L. Meng, Y. Zhang, X. Wan, C. Li, X. Zhang, Y. Wang, X. Ke, Z. Xiao, L. Ding, R. Xia, H.-L. Yip, Y. Cao, and Y. Chen, *Science* **361**, 1094 (2018).
- ²C. J. Brabec, N. S. Sariciftci, and J. C. Hummelen, *Adv. Funct. Mater.* **11**, 15 (2001).
- ³C. J. Brabec, S. Gowrisanker, J. J. M. Halls, D. Laird, S. Jia, and S. P. Williams, *Adv. Mater.* **22**, 3839 (2010).
- ⁴C. W. Tang, *Appl. Phys. Lett.* **48**, 183 (1986).
- ⁵F. C. Krebs, S. A. Gevorgyan, and J. Alstrup, *J. Mater. Chem.* **19**, 5442 (2009).
- ⁶H. J. Park, M. G. Kang, S. H. Ahn, and L. J. Guo, *Adv. Mater.* **22**, E247 (2010).
- ⁷C. N. Hoth, P. Schilinsky, S. A. Choulis, and C. J. Brabec, *Nano Lett.* **8**, 2806 (2008).
- ⁸C. Kim, J. Choi, Y. Bonnassieux, and G. Horowitz, *J. Comput. Electron.* **15**, 1095 (2016).
- ⁹D. Gupta, M. Bag, and K. S. Narayan, *Appl. Phys. Lett.* **92**, 093301 (2008).
- ¹⁰D. Gupta, S. Mukhopadhyay, and K. S. Narayan, *Sol. Energy Mater. Sol. Cells* **94**, 1309 (2010).
- ¹¹M. Glatthaar, M. Riede, N. Keegan, K. Sylvester-Hvid, B. Zimmermann, M. Niggemann, A. Hinsch, and A. Gombert, *Sol. Energy Mater. Sol. Cells* **91**, 390 (2007).
- ¹²W. Tress, A. Petrich, M. Hummert, M. Hein, K. Leo, and M. Riede, *Appl. Phys. Lett.* **98**, 063301 (2011).
- ¹³W. Tress, S. Corvers, K. Leo, and M. Riede, *Adv. Energy Mater.* **3**, 873 (2013).
- ¹⁴J. Bisquert, *Phys. Rev. B* **77**, 235203 (2008).
- ¹⁵L. Burtone, D. Ray, K. Leo, and M. Riede, *J. Appl. Phys.* **111**, 064503 (2012).
- ¹⁶B. Qi and J. Wang, *Phys. Chem. Chem. Phys.* **15**, 8972 (2013).
- ¹⁷W. E. I. Sha, X. Li, and W. C. H. Choy, *Sci. Rep.* **4**, 6236 (2014).
- ¹⁸C. Hyun Kim, O. Yaghmazadeh, Y. Bonnassieux, and G. Horowitz, *J. Appl. Phys.* **110**, 093722 (2011).
- ¹⁹V. D. Mihailetchi, J. Wildeman, and P. W. M. Blom, *Phys. Rev. Lett.* **94**, 126602 (2005).
- ²⁰L. J. A. Koster, E. C. P. Smits, V. D. Mihailetchi, and P. W. M. Blom, *Phys. Rev. B* **72**, 085205 (2005).
- ²¹H. Yu, R. Yi, J. Zhang, A. Yu, H. Peng, J. Qin, and X. Hou, *J. Phys. D Appl. Phys.* **49**, 205105 (2016).
- ²²J. I. Basham, T. N. Jackson, and D. J. Gundlach, *Adv. Energy Mater.* **4**, 1400499 (2014).
- ²³G. Garcia-Belmonte, A. Munar, E. M. Barea, J. Bisquert, I. Ugarte, and R. Pacios, *Org. Electron.* **9**, 847 (2008).
- ²⁴H. Kurt and C. W. Ow-Yang, *Phys. Status Solidi A* **213**, 3165 (2016).
- ²⁵C. H. Kim, K. Kisiel, J. Jung, J. Ulanski, D. Tondelier, B. Geffroy, Y. Bonnassieux, and G. Horowitz, *Synth. Met.* **162**, 460 (2012).
- ²⁶C. Kim, H. Hlaing, S. Yang, Y. Bonnassieux, G. Horowitz, and I. Kymissis, *Org. Electron.* **15**, 1724 (2014).
- ²⁷A. Wagenpfahl, D. Rauh, M. Binder, C. Deibel, and V. Dyakonov, *Phys. Rev. B* **82**, 115306 (2010).
- ²⁸M. B. Upama, M. Wright, B. Puthen-Vettil, N. K. Elumalai, M. A. Mahmud, D. Wang, K. H. Chan, C. Xu, F. Haque, and A. Uddin, *RSC Adv.* **6**, 103899 (2016).
- ²⁹S. John, C. Soukoulis, M. H. Cohen, and E. N. Economou, *Phys. Rev. Lett.* **57**, 1777 (1986).
- ³⁰F. Urbach, *Phys. Rev.* **92**, 1324 (1953).